Available online at www.sciencedirect.com
SCIENCE DIRECT®
Comput. Methods Appl. Mech. Engrg. 195 (2006) 5813–5830
Computer methods in applied mechanics and engineering
www.elsevier.com/locate/cma

Computation of the coupled thermo-optical scattering properties of random particulate systems

T.I. Zohdi *

Department of Mechanical Engineering, 6195 Etcheverry Hall, University of California, Berkeley, CA 94720-1740, USA

Received 24 January 2005; received in revised form 20 April 2005; accepted 21 April 2005

Abstract

The focus of this work is the investigation of the overall scattering behavior of light by aggregates of randomly distributed particles. Specifically, a ray-tracing algorithm is developed and combined with a stochastic genetic algorithm in order to treat coupled inverse optical scattering formulations, where physical parameters, such as particulate volume fractions, refractive indices and thermal constants, are sought so that the aggregate response will match specified coupled scattering, thermal and infrared responses. Large-scale numerical simulations are presented to illustrate the overall procedure and to investigate the propagation through disordered particulate systems.

Keywords: Geometrical optics; Randomly distributed particles; Inverse scattering; Multiple fields

1. Introduction

The scientific analysis of the propagation of radiation, in particular light, is a topic that has matured, since the unification, by Maxwell, in approximately 1865, of the electromagnetic theories of Faraday, Gauss and Ampere. The expressions governing the propagation of electromagnetic waves traveling through space have become known as Maxwell's equations. Virtually all facts about light can be explained in terms of waves.[1] In theory, one could use Maxwell's equations to trace the paths of electromagnetic waves through complex environments. However, when the environment of interest involves hundreds, or thousands, of scatterers, the direct use of Maxwell's equations to describe the flow of energy leads to systems of equations of such complexity that, for all intents and purposes, the problem becomes intractable. A generally simpler approach is based upon *geometrical optics*, which makes use of ray-tracing theory, and which is able to describe various aspects of light propagation, with no concern as to its exact nature. This approach is ideal for high-performance computation associated with the scattering of incident light by multiple particles. An application of particular interest, where scattering calculations can play a supporting role, is the investigation of clustering and aggregation of particles in astrophysical applications where particles collide, cluster, and grow into larger objects. For reviews of such systems, see [9,11,46,7,8,67–69]. For general overviews pertaining to scattering, see [6,60]. For general overviews pertaining to granular media, we refer the reader to a cross-section of that literature: Behringer and collaborators [1–4], Hutter and collaborators [55–57,17,62,5,18,19,25–27,41,24,28], Jaeger and collaborators [29,30,47,43,44,31–35], and Jenkins and collaborators [36–39]. Especially noteworthy are the novel methods for generating extremely high particle volume fractions, which are crucial

* Tel.: +1 510 642 9172; fax: +1 510 642 5539.
E-mail address: zohdi@newton.berkeley.edu

[1] Clearly, some effects, such as those pertaining momentum transfer of incident light, and the resulting "light pressure", can only be explained in terms of photons (packets of energy).

0045-7825/$ - see front matter
doi:10.1016/j.cma.2005.04.023

for the study of randomly packed (high density) granular media, recently developed by Torquato and co-workers, for example, see [16,12–14].

1.1. Ray-theory: scope of use

In this work, we assume that the particle sizes are much greater than the wavelength of the incident light, thus allowing the use of geometrical optics (ray-theory). Large particles dictate a way of looking at scattering problems that is quite different from that of scattering due to small particles, where a variety of other techniques are more appropriate (see [6,15,60]). In ray theory, an incident beam of light may be thought to consist of separate rays of light, each of which travel along their own path. Typically, for a particle of radius 10 or more times the size of the wavelength of light, it is possible to distinguish quite clearly between the rays incident on the particle and rays passing around the particle. Furthermore, experimentally speaking, it is possible to distinguish between rays hitting various parts of the particle's surface. Thus, the rays may be idealized as being localized (Fig. 1).

One can think of geometrical optics as the limiting case of wave optics where the wavelength (λ) tends toward zero, and as being an approximation to Maxwell's equations, in the same spirit as Maxwell's equations are an approximation to quantum mechanics models. In other words, classical mechanics is precisely the same limiting approximation to quantum mechanics as geometrical optics is to wave propagation. Essentially, in geometrical optics, the phase of the wave is considered irrelevant. Thus, for ray-tracing to be a valid approach, the wavelengths should be much smaller than those associated with the length-scales of the scatterers of the problem at hand (Fig. 1).

Remark 1. For visible light, $0.7 \times 10^{-7}\ \text{m} \leqslant \lambda \leqslant 4 \times 10^{-7}\ \text{m}$. Note that all electromagnetic radiation travels at the speed of light in a vacuum, $c \approx 3 \times 10^{8}$ m/s. A more precise value, given by the National Bureau of Standards, is $c \approx 2.997924562 \times 10^{8} \pm 1.1$ m/s.

Remark 2. If the particle sizes are comparable to the wavelength of light, then it is inappropriate to use ray-representations. Rayleigh scattering occurs when the scattering particles are smaller than the wavelength of light. Such scattering occurs when light propagates through gases. For example, when sunlight travels through the Earth's atmosphere, the light appears to be blue because blue light is more thoroughly scattered than other wavelengths of light. For particle sizes that are on the order of the wavelength of light, the regime is Mie scattering. We do not consider such systems in this work. See [6,60] for more details.

1.2. Beams comprised of multiple rays

In ray-tracing methodology, an incident beam of light, which forms a plane-wave front, which is considered "infinite" in extent (in the lateral directions), relative to the wavelength of light, and can be thought of as being comprised of separate rays of light, each of which pursues its own path. Thus, it almost goes without saying that the width of a beam (w) must satisfy $w \gg \lambda$ for the representation as multiple rays to make sense (Fig. 1). One can consider the representation of a beam by multiple rays as simply taking a large "sampling" of the diffraction by the beam (wave front) over the portion of the scatterer where the beam is incident. The trajectory of harmonic plane waves, and the corresponding ray-representation direction, can actually be derived from Maxwell's equations, which reduce to the classical amplitude and trajectory "Eikonal" equations. For more details see [6,15,60].

1.3. Objectives of this paper

We consider initially coherent beams, representing plane-harmonic waves (Fig. 2), composed of multiple collinear rays, where each ray is a vector in the direction of the flow of electromagnetic energy, which, in isotropic media, corresponds to

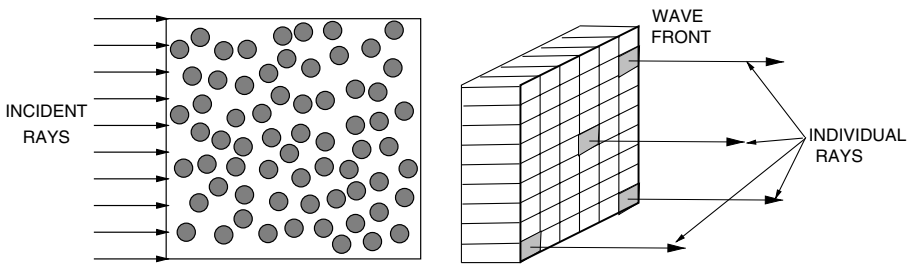

Fig. 1. The multiparticle scattering system considered (left), comprised of a beam (right), comprised of multiple rays, incident on a collection of randomly distributed scatterers.

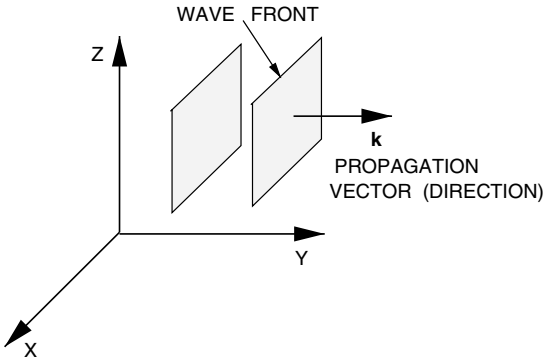

Fig. 2. A wave front and propagation vector.

the normal to the wave front. Thus, for isotropic media, the rays are parallel to the wave's propagation vector, denoted $\boldsymbol{k}$ (Fig. 2). Of particular interest is to describe the break-up of initially highly directional coherent beams, which, under normal circumstances, do not spread out into multidirectional rays. A prime example is highly intense light, such as that associated with lasers.

In the past, a primary drawback of using a geometrical optics approach has been that it is computationally intensive to track multiple rays, undergoing multiple reflections, energy losses to scatterers, generation of heat, etc. Thus, until relatively recently, the problem of a beam of light, comprised of multiple rays, encountering multiple scatters, has been essentially intractable. However, recent simultaneous advances in numerical methods, coupled with the enormous increase in computational power, has led to the possibility that such problems are accessible to rapid desk top computing. Accordingly, in this paper, a ray-tracing algorithm is developed and combined with a stochastic genetic algorithm in order to treat coupled inverse optical scattering formulations, where physical parameters, such as particulate volume fractions, refractive indices and thermal constants, are sought so that the aggregate response will match specified coupled scattering and thermal responses. Large-scale numerical simulations are presented to illustrate the overall procedure and to investigate the propagation through disordered particulate systems.

2. Plane harmonic electromagnetic waves

2.1. Plane waves

We recall the basic form of the wave equation

$$\frac{\partial^2 A}{\partial x^2}+\frac{\partial^2 A}{\partial y^2}+\frac{\partial^2 A}{\partial z^2}=\frac{1}{v^2}\frac{\partial^2 A}{\partial t^2}, \tag{2.1}$$

where A is a variable, and v is the wave speed. We consider time-harmonic plane wave solutions, i.e., those solutions of the form

$$A(\boldsymbol{r},t)=A_0\cos(\boldsymbol{k}\cdot\boldsymbol{r}-\omega t), \tag{2.2}$$

where $\boldsymbol{r}$ is an initial position vector to the wave front, where $\boldsymbol{k}$ is in the direction of propagation. For plane waves, $\boldsymbol{k}\cdot\boldsymbol{r}=$ constant. We refer to the phase as

$$\phi=\boldsymbol{k}\cdot\boldsymbol{r}-\omega t, \tag{2.3}$$

and $\omega=\frac{2\pi}{\tau}$ as the angular frequency, where τ is the period. The wave-front, over which the phase is constant, is a plane for "plane waves", and is orthogonal to the direction of propagation.

2.2. Electromagnetic waves

As we have indicated, the propagation of light can be described via an electromagnetic formalism, via Maxwell's equations (in simplified form), in free space[2]

$$\nabla\times\boldsymbol{E}=-\mu_0\frac{\partial\boldsymbol{H}}{\partial t},\quad \nabla\times\boldsymbol{H}=\epsilon_0\frac{\partial\boldsymbol{E}}{\partial t},\quad \nabla\cdot\boldsymbol{H}=0\quad\text{and}\quad\nabla\cdot\boldsymbol{E}=0, \tag{2.4}$$

[2] See Appendix A for a more general set of relations.

where $\boldsymbol{E}$ is the electric field intensity, where $\boldsymbol{H}$ is the magnetic flux intensity, where ϵ_0 is the permittivity and μ_0 is the permeability. Using standard vector identities, one can show that (see Appendix A)

$$\nabla \times (\nabla \times \boldsymbol{E}) = -\mu_0 \epsilon_0 \frac{\partial^2 \boldsymbol{E}}{\partial t^2} \quad \text{and} \quad \nabla \times (\nabla \times \boldsymbol{H}) = -\mu_0 \epsilon_0 \frac{\partial^2 \boldsymbol{H}}{\partial t^2}, \tag{2.5}$$

and that

$$\nabla^2 \boldsymbol{E} = \frac{1}{c^2} \frac{\partial^2 \boldsymbol{E}}{\partial t^2} \quad \text{and} \quad \nabla^2 \boldsymbol{H} = \frac{1}{c^2} \frac{\partial^2 \boldsymbol{H}}{\partial t^2}, \tag{2.6}$$

and that, employing a Cartesian coordinate system,

$$\frac{\partial^2 E_x}{\partial x^2} + \frac{\partial^2 E_x}{\partial y^2} + \frac{\partial^2 E_x}{\partial z^2} = \frac{1}{c^2} \frac{\partial^2 E_x}{\partial t^2}, \tag{2.7}$$

where $c = \frac{1}{\sqrt{\epsilon_0 \mu_0}}$, with identical relations holding for E_y, E_z, H_x, H_y and H_z. In the case of plane harmonic waves, for example of the form

$$\boldsymbol{E} = \boldsymbol{E}_0 \cos(\boldsymbol{k} \cdot \boldsymbol{r} - \omega t) \quad \text{and} \quad \boldsymbol{H} = \boldsymbol{H}_0 \cos(\boldsymbol{k} \cdot \boldsymbol{r} - \omega t), \tag{2.8}$$

we have

$$\boldsymbol{k} \times \boldsymbol{E} = \mu_0 \omega \boldsymbol{H} \quad \text{and} \quad \boldsymbol{k} \times \boldsymbol{H} = -\epsilon_0 \omega \boldsymbol{E}, \tag{2.9}$$

and

$$\boldsymbol{k} \cdot \boldsymbol{E} = 0 \quad \text{and} \quad \boldsymbol{k} \cdot \boldsymbol{H} = 0. \tag{2.10}$$

The three vectors, $\boldsymbol{k}$, $\boldsymbol{E}$ and $\boldsymbol{H}$ constitute a mutually orthogonal triad. The direction of ray propagation is given by $\frac{\boldsymbol{E} \times \boldsymbol{H}}{\|\boldsymbol{E} \times \boldsymbol{H}\|}$. Since the free space propagation velocity is given by $c = \frac{1}{\sqrt{\epsilon_0 \mu_0}}$ for an electromagnetic wave in a vacuum, and $v = \frac{1}{\sqrt{\epsilon \mu}}$ for electromagnetic waves in another medium, we can define the index of refraction as

$$n \overset{\text{def}}{=} \frac{c}{v} = \sqrt{\frac{\epsilon \mu}{\epsilon_0 \mu_0}}. \tag{2.11}$$

2.3. Optical energy propagation

Light waves traveling through space carry electromagnetic energy which flows in the direction of wave propagation. The energy per unit area per unit time flowing perpendicularly into a surface in free space is given by the Poynting vector $\boldsymbol{S}$, where

$$\boldsymbol{S} = \boldsymbol{E} \times \boldsymbol{H}. \tag{2.12}$$

Since at optical frequencies $\boldsymbol{E}$, $\boldsymbol{H}$ and $\boldsymbol{S}$ oscillate rapidly, it is impractical to measure instantaneous values of $\boldsymbol{S}$ directly. Now consider the harmonic representations in Eq. (2.8) which leads to

$$\boldsymbol{S} = \boldsymbol{E}_0 \times \boldsymbol{H}_0 \cos^2(\boldsymbol{k} \cdot \boldsymbol{r} - \omega t), \tag{2.13}$$

and, consequently, the average value over a longer (but still quite short) time interval than that of the time scale of rapid random oscillation,

$$\langle \boldsymbol{S} \rangle_{\mathscr{T}} = \boldsymbol{E}_0 \times \boldsymbol{H}_0 \langle \cos^2(\boldsymbol{k} \cdot \boldsymbol{r} - \omega t) \rangle_{\mathscr{T}} = \tfrac{1}{2} \boldsymbol{E}_0 \times \boldsymbol{H}_0, \tag{2.14}$$

where $\langle (\cdot) \rangle_{\mathscr{T}} \overset{\text{def}}{=} \frac{1}{\mathscr{T}} \int_0^{\mathscr{T}} (\cdot)\, \mathrm{d}t$. We define the irradiance as

$$I \overset{\text{def}}{=} \langle \|\boldsymbol{S}\| \rangle_{\mathscr{T}} = \frac{1}{2} \|\boldsymbol{E}_0 \times \boldsymbol{H}_0\| = \frac{1}{2} \sqrt{\frac{\epsilon_0}{\mu_0}} \|\boldsymbol{E}_0\|^2. \tag{2.15}$$

Thus, the rate of flow of energy is proportional to the square of the amplitude of the electric field. Furthermore, in isotropic media, which consider for the duration of the work, the direction of energy is in the direction of $\boldsymbol{S}$ and in the same direction as $\boldsymbol{k}$. Since I is the energy per unit area per unit time, if we multiply by the "cross-sectional" area of the ray, a_r, we obtain the energy associated with the ray, denoted as $I a_r = I a_b / N_r$, where a_b is the cross-sectional area of a beam (comprising all of the rays) and N_r is the number of rays in the beam.

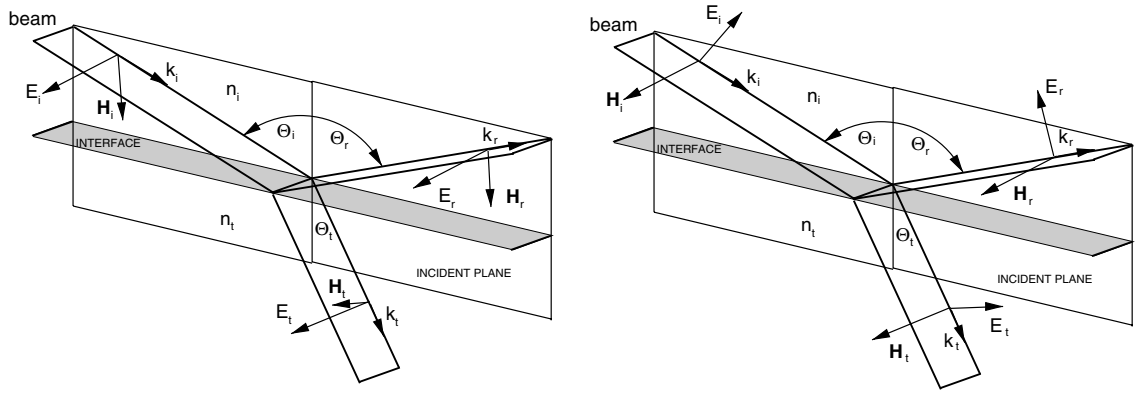

Fig. 3. The nomenclature for Fresnel's equations for the case where the electric field vectors that are (left) perpendicular to the plane of incidence and (right) parallel to the plane of incidence.

2.4. Reflection and absorption of energy

Now we consider a plane harmonic wave incident upon a plane boundary separating two optically different materials, which produces a reflected wave and a transmitted (refracted) wave (Fig. 3). The space-time dependence of the three waves is given by (1) $e^{j(\boldsymbol{k}_i\cdot\boldsymbol{r}-\omega t)}$ for the incident wave (with propagation vector $\boldsymbol{k}_i$), (2) $e^{j(\boldsymbol{k}_r\cdot\boldsymbol{r}-\omega t)}$ for the reflected wave (with propagation vector $\boldsymbol{k}_r$), and (3) $e^{j(\boldsymbol{k}_t\cdot\boldsymbol{r}-\omega t)}$ for the transmitted wave (with propagation vector $\boldsymbol{k}_t$). In order for a time-invariant relation to hold for all points on the boundary, and for all values of t, we must have that the arguments of the exponential function be equal on the boundary. Therefore, since the ωt terms are the same, we have, at the boundary, $\boldsymbol{k}_i\cdot\boldsymbol{r}=\boldsymbol{k}_r\cdot\boldsymbol{r}=\boldsymbol{k}_t\cdot\boldsymbol{r}$, which implies that the waves are coplanar and that their projection onto the plane boundary is equal. We call the plane that contains all three waves the incident plane. Consequently, we have a relation between the propagation constants' magnitudes, $k_i\sin\theta_i=k_r\sin\theta_r=k_t\sin\theta_t$, which implies, because the reflected and incident medium are the same, $\theta_i=\theta_r$. By taking the ratio of the magnitudes of the propagation constants of the transmitted wave and the incident wave, we have

$$\frac{k_t}{k_i}=\frac{\omega/v_t}{\omega/v_i}=\frac{c/v_t}{c/v_i}=\frac{n_t}{n_i}\stackrel{\text{def}}{=}\hat{n}. \tag{2.16}$$

Therefore, we have

$$\frac{\sin\theta_i}{\sin\theta_t}=\hat{n}, \tag{2.17}$$

which is sometimes referred to as the law of refraction. To compute the amount of energy transmitted (absorbed) and reflected by electromagnetic waves, let $\boldsymbol{E}_i$ now denote the (vectorial) amplitude of a plane harmonic wave that is incident on a plane boundary separating two materials. Also, let $\boldsymbol{E}_r$ and $\boldsymbol{E}_t$ be the amplitudes of the reflected and transmitted waves respectively. Eqs. (2.9) and (2.10) collapse to, for the incident, reflected and transmitted magnetic waves

$$\boldsymbol{H}_i=\frac{1}{\mu_i\omega}\boldsymbol{k}_i\times\boldsymbol{E}_i,\quad \boldsymbol{H}_r=\frac{1}{\mu_r\omega}\boldsymbol{k}_r\times\boldsymbol{E}_r\quad\text{and}\quad \boldsymbol{H}_t=\frac{1}{\mu_t\omega}\boldsymbol{k}_t\times\boldsymbol{E}_t. \tag{2.18}$$

Let us now consider an oblique angle of incidence. Consider two cases for the electric field vector: (1) electric field vectors that are parallel ($\|$) to the plane of incidence and (2) electric field vectors that are perpendicular ($\perp$) to the plane of incidence. In either case, the tangential components of the electric and magnetic fields are required to be continuous across the interface. Consider case (1). We have the following general vectorial representations

$$\boldsymbol{E}_\|=E_\|\cos(\boldsymbol{k}\cdot\boldsymbol{r}-\omega t)\boldsymbol{e}_1\quad\text{and}\quad \boldsymbol{H}_\|=H_\|\cos(\boldsymbol{k}\cdot\boldsymbol{r}-\omega t)\boldsymbol{e}_2, \tag{2.19}$$

where $\boldsymbol{e}_1$ and $\boldsymbol{e}_2$ are orthogonal to the propagation direction $\boldsymbol{k}$, and where $E_\|$ and $H_\|$ are the amplitudes of the parallel field components. By employing the law of refraction ($n_i\sin\theta_i=n_t\sin\theta_t$) we obtain the following conditions relating the incident, reflected and transmitted components of the electric field quantities

$$E_{\|i}\cos\theta_i-E_{\|r}\cos\theta_r=E_{\|t}\cos\theta_t\quad\text{and}\quad H_{\perp i}+H_{\perp r}=H_{\perp t}. \tag{2.20}$$

Since, for plane harmonic waves, the magnetic and electric field amplitudes are related by $H=\frac{E}{v\mu}$, we then have

$$E_{\|i}+E_{\|r}=\frac{\mu_i}{\mu_t}\frac{v_i}{v_t}E_{\|t}=\frac{\mu_i}{\mu_t}\frac{n_t}{n_i}E_{\|t}\stackrel{\text{def}}{=}\frac{\hat{n}}{\hat{\mu}}E_{\|t}, \tag{2.21}$$

where $\hat{\mu} \stackrel{\text{def}}{=} \frac{\mu_t}{\mu_i}$, $\hat{n} \stackrel{\text{def}}{=} \frac{n_t}{n_i}$ and where v_i, v_r and v_t are the values of the velocity in the incident, reflected and transmitted directions.[3] By again employing the law of refraction, we obtain the Fresnel reflection and transmission coefficients, generalized for the case of unequal magnetic permeabilities

$$r_{\parallel} = \frac{E_{\parallel r}}{E_{\parallel i}} = \frac{\frac{\hat{n}}{\hat{\mu}}\cos\theta_i - \cos\theta_t}{\frac{\hat{n}}{\hat{\mu}}\cos\theta_i + \cos\theta_t} \quad \text{and} \quad t_{\parallel} = \frac{E_{\parallel t}}{E_{\parallel i}} = \frac{2\cos\theta_i}{\cos\theta_t + \frac{\hat{n}}{\hat{\mu}}\cos\theta_i}. \tag{2.22}$$

Following the same procedure for case (2), where the components of $\boldsymbol{E}$ are perpendicular to the plane of incidence, we have

$$r_{\perp} = \frac{E_{\perp r}}{E_{\perp i}} = \frac{\cos\theta_i - \frac{\hat{n}}{\hat{\mu}}\cos\theta_t}{\cos\theta_i + \frac{\hat{n}}{\hat{\mu}}\cos\theta_t} \quad \text{and} \quad t_{\perp} = \frac{E_{\perp t}}{E_{\perp i}} = \frac{2\cos\theta_i}{\cos\theta_i + \frac{\hat{n}}{\hat{\mu}}\cos\theta_t}. \tag{2.23}$$

Our primary interest is in the reflections. We define the reflectances as

$$R_{\parallel} \stackrel{\text{def}}{=} r_{\parallel}^2 \quad \text{and} \quad R_{\perp} \stackrel{\text{def}}{=} r_{\perp}^2. \tag{2.24}$$

Particularly convenient forms for the reflections are

$$r_{\parallel} = \frac{\frac{\hat{n}^2}{\hat{\mu}}\cos\theta_i - (\hat{n}^2 - \sin^2\theta_i)^{\frac{1}{2}}}{\frac{\hat{n}^2}{\hat{\mu}}\cos\theta_i + (\hat{n}^2 - \sin^2\theta_i)^{\frac{1}{2}}} \quad \text{and} \quad r_{\perp} = \frac{\cos\theta_i - \frac{1}{\hat{\mu}}(\hat{n}^2 - \sin^2\theta_i)^{\frac{1}{2}}}{\cos\theta_i + \frac{1}{\hat{\mu}}(\hat{n}^2 - \sin^2\theta_i)^{\frac{1}{2}}}. \tag{2.25}$$

Thus, the total energy reflected can be characterized by

$$R \stackrel{\text{def}}{=} \left(\frac{E_r}{E_i}\right)^2 = \frac{E_{\perp r}^2 + E_{\parallel i}^2}{E_i^2} = \frac{I_{\parallel r} + I_{\perp r}}{I_i}. \tag{2.26}$$

If the resultant plane of oscillation of the (polarized) wave makes an angle of γ_i with the plane of incidence, then

$$E_{\parallel i} = E_i\cos\gamma_i \quad \text{and} \quad E_{\perp i} = E_i\sin\gamma_i, \tag{2.27}$$

and it follows from the previous definition of I that

$$I_{\parallel i} = I_i\cos^2\gamma_i \quad \text{and} \quad I_{\perp i} = I_i\sin^2\gamma_i. \tag{2.28}$$

Substituting these expression back into the expressions for the reflectances yields

$$R = \frac{I_{\parallel r}}{I_i}\cos^2\gamma_i + \frac{I_{\perp r}}{I_i}\sin^2\gamma_i = R_{\parallel}\cos^2\gamma_i + R_{\perp}\sin^2\gamma_i. \tag{2.29}$$

For natural or unpolarized light, the angle γ_i varies rapidly in a random manner, as does the field amplitude. Thus, since

$$\langle\cos^2\gamma_i(t)\rangle_{\mathscr{T}} = \tfrac{1}{2} \quad \text{and} \quad \langle\sin^2\gamma_i(t)\rangle_{\mathscr{T}} = \tfrac{1}{2}, \tag{2.30}$$

and therefore for natural light

$$I_{\parallel i} = \frac{I_i}{2} \quad \text{and} \quad I_{\perp i} = \frac{I_i}{2}, \tag{2.31}$$

and therefore

$$r_{\parallel}^2 = \left(\frac{E_{\parallel r}^2}{E_{\parallel i}^2}\right)^2 = \frac{I_{\parallel r}}{I_{\parallel i}} \quad \text{and} \quad r_{\perp}^2 = \left(\frac{E_{\perp r}^2}{E_{\perp i}^2}\right)^2 = \frac{I_{\perp r}}{I_{\perp i}}. \tag{2.32}$$

Thus, the total reflectance becomes

$$R = \tfrac{1}{2}(R_{\parallel} + R_{\perp}) = \tfrac{1}{2}(r_{\parallel}^2 + r_{\perp}^2), \tag{2.33}$$

where $0 \leqslant R \leqslant 1$.

Remark 1. For almost all known materials the magnetic permeability is, within experimental measurements, virtually the same.[4] For the remainder of the work, we shall take $\hat{\mu} = 1$, i.e., $\mu_0 = \mu_i \approx \mu_t$.

[3] Throughout the analysis we assume that $\hat{n} \geqslant 1$.

[4] A few notable exceptions are concentrated magnetite, pyrrhotite, and titanomagnetite [58,48].

Remark 2. For the cases where $\sin\theta_t = \frac{\sin\theta_i}{\hat{n}} > 1$, one may rewrite reflection relations as

$$r_{\parallel} = \frac{\frac{\hat{n}^2}{\hat{\mu}}\cos\theta_i - \mathrm{j}(\sin^2\theta_i - \hat{n}^2)^{\frac{1}{2}}}{\frac{\hat{n}^2}{\hat{\mu}}\cos\theta_i + \mathrm{j}(\sin^2\theta_i - \hat{n}^2)^{\frac{1}{2}}} \quad \text{and} \quad r_{\perp} = \frac{\cos\theta_i - \frac{1}{\hat{\mu}}\mathrm{j}(\sin^2\theta_i - \hat{n}^2)^{\frac{1}{2}}}{\cos\theta_i + \frac{1}{\hat{\mu}}\mathrm{j}(\sin^2\theta_i - \hat{n}^2)^{\frac{1}{2}}}, \tag{2.34}$$

where, $\mathrm{j} = \sqrt{-1}$, and in this complex case[5]

$$R_{\parallel} \stackrel{\text{def}}{=} r_{\parallel}\bar{r}_{\parallel} = 1 \quad \text{and} \quad R_{\perp} \stackrel{\text{def}}{=} r_{\perp}\bar{r}_{\perp} = 1, \tag{2.35}$$

where $\bar{r}_{\parallel}$ and $\bar{r}_{\perp}$ are complex conjugates. Thus, for angles below the critical angle θ_i^*, all of the energy is reflected.

Remark 3. Notice that as $\hat{n} \to 1$ we have complete absorption, while as $\hat{n} \to \infty$ we have complete reflection. The total amount of absorbed power by the particles is $(1 - R)I_i$. As mentioned previously, the medium surrounding the particles is assumed to behave as a vacuum, i.e., there are no energetic losses as the electromagnetic rays pass through it. However, we assume that all electromagnetic energy that is absorbed from a ray by a particle is converted into heat, and that no electromagnetic rays are refracted (and emitted) or dispersed. Heat generation and accompanying infrared radiation emission (with wavelengths in the ranges of $10^{-7}\,\mathrm{m} \leqslant \lambda \leqslant 10^{-4}\,\mathrm{m}$) is addressed next.

3. Thermal coupling

Throughout the thermal analysis, we shall use the most simplified models possible. It is assumed scattering particles are small enough to consider that the temperature fields are uniform in the particles.[6] We consider an energy balance, governing the interconversions of mechanical, thermal and chemical energy in a system, dictated by the First Law of Thermodynamics. Accordingly, we require the time rate of change of the sum of the kinetic energy ($\mathscr{K}$) and stored energy ($\mathscr{S}$) to be equal to the work rate (power, $\mathscr{P}$) and the net heat supplied ($\mathscr{H}$)

$$\frac{\mathrm{d}}{\mathrm{d}t}(\mathscr{K} + \mathscr{S}) = \mathscr{P} + \mathscr{H}, \tag{3.1}$$

where the stored energy is comprised of a thermal part, $\mathscr{S}(t) = mC\theta(t)$, where C is the heat capacity per unit mass, and, consistent with our assumptions that the particles deform negligibly during the process, *a negligible mechanical stored energy portion*. The kinetic energy is $\mathscr{K}(t) = \frac{1}{2}m\boldsymbol{v}(t)\cdot\boldsymbol{v}(t)$. The mechanical power term is due to the total forces ($\boldsymbol{\Psi}^{\text{tot}}$) acting on a particle

$$\mathscr{P} = \frac{\mathrm{d}\mathscr{W}}{\mathrm{d}t} = \boldsymbol{\Psi}^{\text{tot}}\cdot\boldsymbol{v}, \tag{3.2}$$

and, because $\frac{\mathrm{d}\mathscr{K}}{\mathrm{d}t} = m\dot{\boldsymbol{v}}\cdot\boldsymbol{v}(t)$, and a balance of momentum $m\dot{\boldsymbol{v}}\cdot\boldsymbol{v} = \boldsymbol{\Psi}^{\text{tot}}\cdot\boldsymbol{v}$ and thus $\frac{\mathrm{d}\mathscr{K}}{\mathrm{d}t} = \frac{\mathrm{d}\mathscr{W}}{\mathrm{d}t} = \mathscr{P}$, leading to $\frac{\mathrm{d}\mathscr{S}}{\mathrm{d}t} = \mathscr{H}$. The primary source of heat is due to the incident rays. The energy input from the reflection of a ray is defined as

$$\Delta\mathscr{H}^{\text{rays}} \stackrel{\text{def}}{=} \int_t^{t+\Delta t} \mathscr{H}^{\text{rays}}\,\mathrm{d}t \approx (I_i - I_r)a_r\Delta t = (1 - R)I_i a_r\Delta t. \tag{3.3}$$

After an incident ray is reflected, it is assumed that a process of heat transfer transpires. It is assumed that the temperature fields are uniform within the particles, thus conduction within the particles is negligible. We remark that the validity of using a lumped thermal model, i.e., ignoring temperature gradients and assuming a uniform temperature within a particle, is dictated by the magnitude of the Biot number. A small Biot number indicates that such an approximation is reasonable. The Biot number for spheres scales with the ratio of particle volume (V) to particle surface area (a_s), $\frac{V}{a_s} = \frac{b}{3}$, which indicates that a uniform temperature distribution is appropriate, since the particles, by definition, are small (Fig. 4).

The First Law reads

$$\frac{\mathrm{d}(K+S)}{\mathrm{d}t} = m\dot{\boldsymbol{v}}\cdot\boldsymbol{v} + mC\dot{\theta} = \underbrace{\boldsymbol{\Psi}^{\text{tot}}\cdot\boldsymbol{v}}_{\text{mechanical power}} - \underbrace{h_c a_s(\theta - \theta_0)}_{\text{convective heating}} - \underbrace{\mathscr{B}a_s\varepsilon(\theta^4 - \theta_s^4)}_{\text{thermal radiation}} + \underbrace{\mathscr{H}^{\text{rays}}}_{\text{sources}}, \tag{3.4}$$

where θ_0 is the temperature of the ambient environment, where θ_s is the temperature of the far field surface (for example a container surrounding the flow) with which radiative exchange is made, $\mathscr{B} = 5.67\times10^{-8}\frac{W}{m^2-K}$ is the Stefan–Boltzmann

[5] The limiting case $\frac{\sin\theta_i^*}{\hat{n}} = 1$, is the critical angle (θ_i^*) case.

[6] Thus, the gradient of the temperature within the particle is zero, i.e., $\nabla\theta = \boldsymbol{0}$. Thus, a Fourier-type law for the heat flux will register a zero value, $\boldsymbol{q} = -\cdot\nabla\theta = \boldsymbol{0}$. Furthermore, we assume that the space between the particles, i.e., the "ether", plays no role in the heat transfer process.

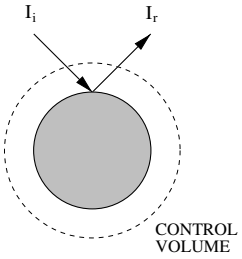

Fig. 4. Control volume for heat transfer.

constant, where $0 \leqslant \varepsilon \leqslant 1$ is the emissivity, which indicates how efficiently the surface radiates energy compared to a blackbody (an ideal emitter), where $0 \leqslant h_c$ is the heating due to convection (Newton's Law of cooling) into the environment and where a_s is the surface area of a particle. *It is assumed that the thermal radiation exchange between the particles is negligible.* For the applications considered presently, typically, h_c is quite small, and play a small role in the heat transfer processes. From a balance of momentum we have $m\dot{\boldsymbol{v}} \cdot \boldsymbol{v} = \boldsymbol{\Psi}^{\text{tot}} \cdot \boldsymbol{v}$ and Eq. (3.4) becomes

$$mC\dot{\theta} = -h_c a_s(\theta - \theta_0) - \mathscr{B} a_s \varepsilon(\theta^4 - \theta_s^4) + \mathscr{H}^{\text{rays}}. \tag{3.5}$$

Therefore, after temporal integration with a finite difference time-step of Δt we have

$$\theta(t + \Delta t) = \frac{1}{mC + h_c a_s \Delta t}\left(mC\theta(t) - \Delta t \mathscr{B} a_s \varepsilon(\theta^4(t + \Delta t) - \theta_s^4) + \Delta t h_c a_s \theta_0 + \Delta \mathscr{H}^{\text{rays}}\right). \tag{3.6}$$

This implicit nonlinear equation for θ, *for each particle*, is added into ray-tracing algorithm in the next section.

Remarks. For the cases considered presently, convection plays an insignificant role in the heat transfer process. Thus, we shall neglect it, although we retain the term in the equations for generality. Also, we recall that a blackbody is an ideal radiating surface having the following properties:

- A blackbody absorbs all incident radiation, regardless of wavelength and direction,
- For a prescribed temperature and wavelength, no surface can emit more energy than a blackbody and
- Although the radiation emitted by a blackbody is a function of wavelength and temperature, it is independent of direction.

Since a blackbody is a perfect emitter, it serves as a standard against which the radiative properties of actual surfaces may be compared. The Stefan–Boltzmann law, which is computed by integrating the Planck representation of the emissive power distribution of a blackbody over all wavelengths, allows the calculation of the amount of radiation emitted in all directions and over all wavelengths simply from the knowledge of the temperature of the blackbody.

4. Solution procedure

We now develop a staggering scheme by extending an approach found in [63–65,67,68]. After time discretization of the stored energy term in the equations of thermal equilibrium for a particle

$$mC\dot{\theta}_i^{L+1} \approx mC\frac{\theta_i^{L+1} - \theta_i^L}{\Delta t}, \tag{4.1}$$

where, for brevity, we denote $\theta_i^{L+1} \stackrel{\text{def}}{=} \theta_i(t + \Delta t)$, $\theta_i^L \stackrel{\text{def}}{=} \theta_i(t)$, etc., one can arrive at the following abstract form, for the entire system, $\mathscr{A}(\theta_i^{L+1}) = \mathscr{F}$. It is convenient to write

$$\mathscr{A}(\theta_i^{L+1}) - \mathscr{F} = \mathscr{G}(\theta_i^{L+1}) - \theta_i^{L+1} + \mathscr{E} = 0, \tag{4.2}$$

where $\mathscr{E}$ is a remainder term which does not depend on the solution, i.e., $\mathscr{E} \neq \mathscr{E}(\theta_i^{L+1})$. A straightforward iterative scheme can be written as

$$\theta_i^{L+1,K} = \mathscr{G}(\theta_i^{L+1,K-1}) + \mathscr{E}, \tag{4.3}$$

where $K = 1, 2, 3, \ldots$ is the index of iteration within time-step $L + 1$. The convergence of such a scheme is dependent on the behavior of $\mathscr{G}$. Namely, a sufficient condition for convergence is that $\mathscr{G}$ is a contraction mapping for all $\theta_i^{L+1,K}$, $K = 1, 2, 3, \ldots$ In order to investigate this further, we define the error as $\Delta\theta^{L+1,K} = \theta_i^{L+1,K} - \theta_i^{L+1}$. A necessary restriction for convergence is iterative self consistency, i.e., the exact solution must be represented by the scheme $\mathscr{G}(\theta_i^{L+1}) + \mathscr{E} = \theta_i^{L+1}$. Enforcing this restriction, a sufficient condition for convergence is the existence of a contraction mapping of the form

$$\|\Delta\theta^{L+1,K}\| = \|\theta_i^{L+1,K} - \theta_i^{L+1}\| = \|\mathscr{G}(\theta_i^{L+1,K-1}) - \mathscr{G}(\theta_i^{L+1})\| \leqslant \eta^{L+1,K}\|\theta_i^{L+1,K-1} - \theta_i^{L+1}\|, \tag{4.4}$$

where, if $\eta^{L+1,K} < 1$ for each iteration K, then $\Delta\,\theta^{L+1,K} \to 0$ for any arbitrary starting value $\theta_i^{L+1,K=0}$ as $K \to \infty$. The type of contraction condition discussed is sufficient, but not necessary, for convergence. Typically, the time-step sizes for ray tracing are far smaller than needed, thus, the approach converges quickly. More specifically, $\mathscr{G}$'s behavior is controlled by $\dfrac{\Delta t \mathscr{B} a_s \varepsilon}{mC + h_c a_s \Delta t}$, which is quite small. Thus, a fixed-point iterative scheme, such as the one introduced, converges rapidly. This iterative procedure is embedded into the overall ray-tracing scheme. The overall algorithm is as follows, starting at $t = 0$ and ending at $t = T$:

(★) COMPUTE RAY ORIENTATIONS AFTER REFLECTION (FRESNEL RELATIONS)
COMPUTE ABSORPTION CONTRIBUTIONS TO THE PARTICLES: $\Delta\mathscr{H}^{\text{rays}}$
COMPUTE PARTICLE TEMPERATURES (RECURSIVELY, $K = 1, 2, \ldots$ UNTIL CONVERGENCE) :
$$\theta^{L+1,K} = \frac{1}{mC + h_c a_s \Delta t}\left(mC\theta^{L} - \Delta t \mathscr{B} a_s \varepsilon\left((\theta^{L+1,K-1})^4 - \theta_s^4\right) + \Delta t h_c a_s \theta_0 + \Delta\mathscr{H}^{\text{rays}}\right)$$
INCREMENT ALL RAY FRONT POSITIONS: $\boldsymbol{r}_i(t + \Delta t) = \boldsymbol{r}_i(t) + \Delta t \boldsymbol{v}_i(t)$
GO TO (★) AND REPEAT $(t = t + \Delta t)$

(4.5)

The time step size Δt is dictated by the size of the particles. A somewhat ad-hoc approach is to scale the time step size according to $\Delta t \propto \frac{\xi b}{\|\boldsymbol{v}\|}$, where b is the radius of the particles, $\|\boldsymbol{v}\|$ is the magnitude of the velocity of the rays and ξ is a scaling factor, typically $0.05 \leqslant \xi \leqslant 0.1$. To compute Π one must go through the procedure in Box (4.5), requiring a full-scale simulation.

5. Inverse problems/parameter identification

An important aspect of any model is the inverse problem of identification of parameters which force the system behavior to match a target response, and which may stem from an experimental observation, or a design specification. In the ideal case, one would like to determine combinations of scattering parameters, which produce certain aggregate effects, via numerical simulations, in order to minimize time-consuming laboratory tests. The primary quantity of interest in this work is the percentage of lost irradiance by a beam in a selected direction over the time interval of $(0, T)$. As in the previous examples, this is characterized by the inner product of the Poynting vector and a selected direction ($\boldsymbol{d}$):

$$\mathscr{Z}(0,T) \stackrel{\text{def}}{=} \frac{\sum_{i=1}^{N_r}(\boldsymbol{S}(t=0) - \boldsymbol{S}(t=T)) \cdot \boldsymbol{d}}{\sum_{i=1}^{N_r}\boldsymbol{S}_i(t=0) \cdot \boldsymbol{d}}, \tag{5.1}$$

where $\mathscr{Z}$ can be considered the amount of energy "blocked" (in a vectorally averaged sense) from propagating in the $\boldsymbol{d}$ direction. Now consider a cost function comparing the loss to the specified blocked amount:

$$\Pi \stackrel{\text{def}}{=} \left|\frac{\mathscr{Z}(0,T) - \mathscr{Z}^*}{\mathscr{Z}^*}\right|, \tag{5.2}$$

where total simulation time is T and where $\mathscr{Z}^*$ is a target blocked value. One can augment this by also monitoring the average temperature of the scattering particles during the time interval,

$$\Theta(0,T) \stackrel{\text{def}}{=} \frac{1}{N_p T}\int_0^T \sum_{i=1}^{N_p}\theta_i(t)\,\mathrm{d}t, \tag{5.3}$$

as well as the average emitted thermal radiation of the scatterers during the time interval

$$\Gamma(0,T) \stackrel{\text{def}}{=} \frac{1}{N_p T}\int_0^T \sum_{i=1}^{N_p}\mathscr{B} a_{si}\varepsilon_i(\theta_i^4(t) - \theta_s^4)\,\mathrm{d}t, \tag{5.4}$$

to yield the following composite cost function

$$\Pi(w_1,w_2,w_3) \stackrel{\text{def}}{=} \frac{1}{\sum_{j=1}^{3} w_j}\left(w_1\left|\frac{\mathscr{Z}(0,T) - \mathscr{Z}^*}{\mathscr{Z}^*}\right| + w_2\left|\frac{\Theta(0,T) - \Theta^*}{\Theta^*}\right| + w_3\left|\frac{\Gamma(0,T) - \Gamma^*}{\Gamma^*}\right|\right), \tag{5.5}$$

where Θ^* and Γ^* are specified values. Typically, for the class of problems considered in this work, formulations such as in Eq. (5.5) depend in a nonconvex and nondifferentiable manner, on the system parameters. With respect to the minimization

of Eq. (5.5), classical gradient-based deterministic optimization techniques are not robust, due to difficulties with objective function nonconvexity and nondifferentiability. Classical gradient-based algorithms are likely to converge only toward a local minimum of the objective functional if an accurate initial guess to the global minimum is not provided. Also, usually it is extremely difficult to construct an initial guess that lies within the (global) convergence radius of a gradient-based method. These difficulties can be circumvented by the use of a certain class of nonderivative search methods, usually termed "genetic" algorithms (GA), before applying gradient-based schemes. Genetic algorithms are search methods based on the principles of natural selection, employing concepts of species evolution, such as reproduction, mutation and crossover. Implementation typically involves a randomly generated population of fixed-length elemental strings, "genetic information", each of which represents a specific choice of system parameters. The population of individuals undergo "mating sequences" and other biologically inspired events in order to find promising regions of the search space. There are a variety of such methods, which employ concepts of species evolution, such as reproduction, mutation and crossover. Such methods primarily stem from the work of John Holland [20]. For reviews of such methods, see, for example, [22,10,49,40,42,50–53,23].

5.1. A specific genetic algorithm for particulate systems

Adopting the approaches found in [63–68], a genetic algorithm has been developed to treat nonconvex inverse problems involving various aspects of multi-particle mechanics. The central idea is that the system parameters form a genetic string and a survival of the fittest algorithm is applied to a population of such strings. The overall process is (a) a population (S members in total) of different parameter sets are generated at random within the parameter space, each represented by a ("genetic") string of the system (N) parameters, (b) the performance of each parameter set is tested, (c) the parameter sets are ranked from top to bottom according to their performance, (d) the best parameter sets (parents) are mated pairwise producing two offspring (children), i.e., each best pair exchanges information by taking random convex combinations of the parameter set components of the parents' genetic strings and (e) the worst performing genetic strings are eliminated, new replacement parameter sets (genetic strings) are introduced into the remaining population of best performing genetic strings and the process (a–e) is then repeated. The term "fitness" of a genetic string is used to indicate the value of the objective function. The most fit genetic string is the one with the smallest objective function. The retention of the top fit genetic strings from a previous generation (parents) is critical, since if the objective functions are highly nonconvex (the present case), there exists a clear possibility that the inferior offspring will replace superior parents. When the top parents are retained, the minimization of the cost function is guaranteed to be monotone (guaranteed improvement) with increasing generations. There is no guarantee of successive improvement if the top parents are not retained, even though nonretention of parents allows more new genetic strings to be evaluated in the next generation. Numerical studies conducted by the author imply that, for sufficiently large populations, the benefits of parent retention outweigh this advantage and any disadvantages of "inbreeding", i.e., a stagnant population. For more details on this "inheritance property", see [10] or [40]. In the upcoming algorithm, inbreeding is mitigated since, with each new generation, new parameter sets, selected at random within the parameter space, are added to the population. Previous numerical studies of the author [65] have indicated that not retaining the parents is suboptimal due to the possibility that inferior offspring will replace superior parents. Additionally, parent retention is computationally less expensive, since these parameter sets do not have to be reevaluated in the next generation.

An implementation of such ideas is as follows [63–68]:

- **Step 1:** Randomly generate a population of S starting genetic strings, $\mathbf{\Lambda}^i$, $i = 1,\ldots,S$:

  $$\mathbf{\Lambda}^i \stackrel{\text{def}}{=} \{\Lambda_1^i, \Lambda_2^i, \Lambda_3^i, \Lambda_4^i, \ldots, \Lambda_N^i\}.$$

- **Step 2:** Compute fitness of each string $\Pi(\mathbf{\Lambda}^i)$, $i = 1,\ldots,S$.
- **Step 3:** Rank genetic strings: $\mathbf{\Lambda}^i$, $i = 1,\ldots,S$.
- **Step 4:** Mate nearest pairs and produce two offspring, $i = 1,\ldots,S$:

  $$\boldsymbol{\lambda}^i \stackrel{\text{def}}{=} \Phi^{(\mathrm{I})}\mathbf{\Lambda}^i + (1-\Phi^{(\mathrm{I})})\mathbf{\Lambda}^{i+1}, \qquad \boldsymbol{\lambda}^{i+1} \stackrel{\text{def}}{=} \Phi^{(\mathrm{II})}\mathbf{\Lambda}^i + (1-\Phi^{(\mathrm{II})})\mathbf{\Lambda}^{i+1}.$$

- **Note:** $\Phi^{(\mathrm{I})}$ and $\Phi^{(\mathrm{II})}$ are random numbers, such that $0 \leqslant \Phi^{(\mathrm{I})}, \Phi^{(\mathrm{II})} \leqslant 1$, which are different for each component of each genetic string.
- **Step 5:** Kill off bottom $M < S$ strings and keep top $K < N$ parents and top K offspring (K offspring + K parents + $M = S$).
- **Step 6:** Repeat Steps 1–6 with top gene pool (K offspring and K parents), plus M new, randomly generated, strings
- **Option:** Rescale and restart search around best performing parameter set every few generations.
- **Option:** We remark that gradient-based methods are sometimes useful for post-processing solutions found with a genetic algorithm, if the objective function is sufficiently smooth in that region of the parameter space. In other words, if one has located convex portion of the parameter space with a global genetic search, one can employ gradient-based procedures

locally to minimize the objective function further. In such procedures, in order to obtain a new directional step for $\mathbf{\Lambda}$, one must solve the following system, $[\mathbb{H}]\{\Delta\mathbf{\Lambda}\} = -\{\boldsymbol{g}\}$, where $[\mathbb{H}]$ is the Hessian matrix ($N \times N$), where $\{\Delta\mathbf{\Lambda}\}$ is the parameter increment ($N \times 1$), and $\{\boldsymbol{g}\}$ is the gradient ($N \times 1$). We shall not employ this second (post-genetic) stage in this work. Reviews of these methods can be found in the texts of Luenberger [45] and Gill et al. [21], while a state of the art can be found in [54].

Remark 1. To compute the fitness of a parameter set one must go through the procedure in Box (4.5), requiring a full-scale simulation. It is important to scale the system variables, for example, to be positive numbers and of comparable magnitude, in order to avoid dealing with large variations in the parameter vector components. Typically, for particulate flows with a finite number of particles, there will be slight variations in the performance for different random starting configurations. In order to stabilize the objective function's value with respect to the randomness of the flow starting configuration, for a given parameter selection ($\mathbf{\Lambda}$), a regularization procedure is applied within the genetic algorithm, whereby the performances of a series of different random starting configurations are averaged until the (ensemble) average converges, i.e., until the following condition is met:

$$\left| \frac{1}{M+1} \sum_{i=1}^{M+1} \Pi^{(i)}(\mathbf{\Lambda}^{\mathrm{I}}) - \frac{1}{M} \sum_{i=1}^{M} \Pi^{(i)}(\mathbf{\Lambda}^{\mathrm{I}}) \right| \leqslant \mathrm{TOL} \left| \frac{1}{M+1} \sum_{i=1}^{M+1} \Pi^{(i)}(\mathbf{\Lambda}^{\mathrm{I}}) \right|,$$

where index i indicates a different starting random configuration ($i = 1, 2, \ldots, M$) that has been generated and M indicates the total number of configurations (samples) tested. In order to implement this in the genetic algorithm, in Step 2, one simply replaces *compute* with *ensemble compute*, which requires a further inner loop to test the performance of multiple starting configurations. Similar ideas have been applied to other types of randomly dispersed particulate media in [63–68]. *Clearly, such a procedure is not necessary when the scatterers are periodically arranged.*

Remark 2. The classical random sequential addition (RSA) algorithm was used to place nonoverlapping particles into the domain of interest [61]. This algorithm was adequate for the volume fraction ranges of interest (under 30%), since its limit is on the order of 38%. To achieve higher volume fractions, there are a variety of more sophisticated algorithms, such as the equilibrium-based Metropolis algorithm. For a detailed review of a variety of such methods (see [59]). For much higher volume fractions, effectively packing (and "jamming") particles to theoretical limits (approximately 74%), a new novel class of methods has recently been developed, based on simultaneous particle flow and growth, by Torquato and coworkers (see, for example, [16,12–14]). This class of methods was not employed in the present study, due to the relatively moderate volume fraction range of interest here, however, such methods appear to offer distinct computational advantages if extremely high volume fractions are desired.

5.2. Parametrization of the scatterers and a genetic algorithm

We considered a group of N_p randomly positioned particles, of equal size, in a cube of normalized dimensions, $D \times D \times D$, with D normalized to unity. The particle size and volume fraction were determined by a particle/sample size ratio, which was defined via a subvolume size $V \stackrel{\mathrm{def}}{=} \frac{D \times D \times D}{N_p}$, where N_p was the number of particles in the entire cube (Fig. 5). The ratio between the radius (b) and the subvolume was denoted by $\mathscr{L} \stackrel{\mathrm{def}}{=} \frac{b}{V^{\frac{1}{3}}}$. The volume fraction occupied by the particles was $v_p \stackrel{\mathrm{def}}{=} \frac{4\pi\mathscr{L}^3}{3}$. Thus, the total volume occupied by the particles, denoted ζ, can be written as $\zeta = v_p N_p V$. We used $N_p = 1000$ particles and $N_r = 400$ rays, arranged in a square 20×20 pattern (Fig. 7). This system provided stable

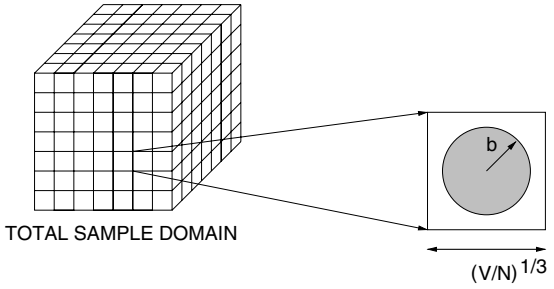

Fig. 5. Definition of a particle length scale.

results, i.e., increasing the number of rays and/or the number of particles beyond these levels resulted in negligibly different overall system responses. The free parameters in the inverse problem were:

- The particle length scale of $0 < \mathscr{L} \leqslant 0.35$,
- The relative refractive index ratio $1 < \hat{n} \leqslant 10$,
- The particle emissivity $0 \leqslant \varepsilon \leqslant 1$,
- The particle density, combined with the heat capacity, $(\rho C)^- \leqslant (\rho C) \leqslant (\rho C)^+$, which dictates the mass via $m = \rho \frac{4}{3}\pi b^3$. C was held fixed at $C = 10^3$ N m/K and 10^3 kg/m^3 $= \rho^- \leqslant \rho \leqslant \rho^+ = 2 \times 10^3$ kg/m^3.

Thus, explicitly, the genetic string was comprised of the following parameters:

$$\mathbf{\Lambda} = (\mathscr{L}, \rho C, \epsilon, \hat{n}). \tag{5.6}$$

Other simulation parameters of importance are

- The dimensions of the sample were 10^{-3} m $\times 10^{-3}$ m $\times 10^{-3}$ m.
- The time-scale was set to $\frac{3\times 10^{-3}\ \mathrm{m}}{c}$, where $c = 3 \times 10^8$ m/s is the speed of light.
- The initial velocity vector for all initially colinear rays comprising the beam was $\boldsymbol{v} = (c, 0, 0)$.
- The irradiance beam parameter was set to $I = 10^{18}$ N m/(m^2 s), where the irradiance for each ray was calculated as $I^{\mathrm{ray}}(t=0)a_r \stackrel{\mathrm{def}}{=} Ia_b/N_r$, where $N_r = 20 \times 20 = 400$ is the number of rays in the beam and $a_b = 10^{-3}$ m $\times 10^{-3}$ m $= 10^{-6}$ m^2 is the cross-sectional area of the beam.
- The first two objectives were $\mathscr{Z}^* = 0.75$ and $\Theta^* = 400$ K. A convenient way to parametrize Γ^* is to write it as a percentage of the incident energy per unit time of the entire beam, $K^* I^{\mathrm{ray}}(t=0) \times N_r$, where $0 \leqslant K^* \leqslant 1$. A value of $K^* = 10^{-18}$ was chosen.

The number of genetic strings in the population was set to 20, for 20 generations, allowing six offspring of the top six parents, along with their parents, to proceed to the next generation. Therefore, after each generation, eight entirely new genetic strings are introduced. Every ten generations, the search was rescaled around the best parameter set, and the search restarted. Table 1 depicts the results. A total of 286 parameter selections were tested. The behavior of the best parameter selection's response is shown in Figs. 6–11. The total number of strings tested was 3651, thus requiring an average of 12.765

Table 1
The optimal scattering parameters and the top six fitnesses with $w_1 = w_2 = w_3 = 1$

Rank	$\mathscr{L}$	$\hat{n}$	ε	$\rho \times 10^{-3}$ kg/m^3	Π
1	0.21480	5.82056	0.53687	0.15078	0.04968310
2	0.21481	5.91242	0.53741	0.15152	0.05126406
3	0.21482	5.89121	0.53637	0.15152	0.05166210
4	0.21482	5.83350	0.53636	0.15150	0.05232877
5	0.21477	6.23032	0.53748	0.16034	0.05236720
6	0.21481	5.81637	0.53672	0.15008	0.05260397

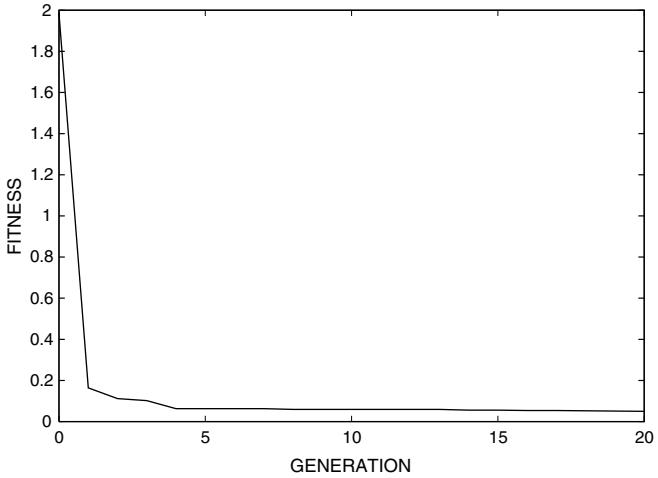

Fig. 6. The best parameter set's objective function values for successive generations. Note: The first data point in the optimization corresponds to the objective function's value for mean parameter values of upper and lower bounds of the search intervals.

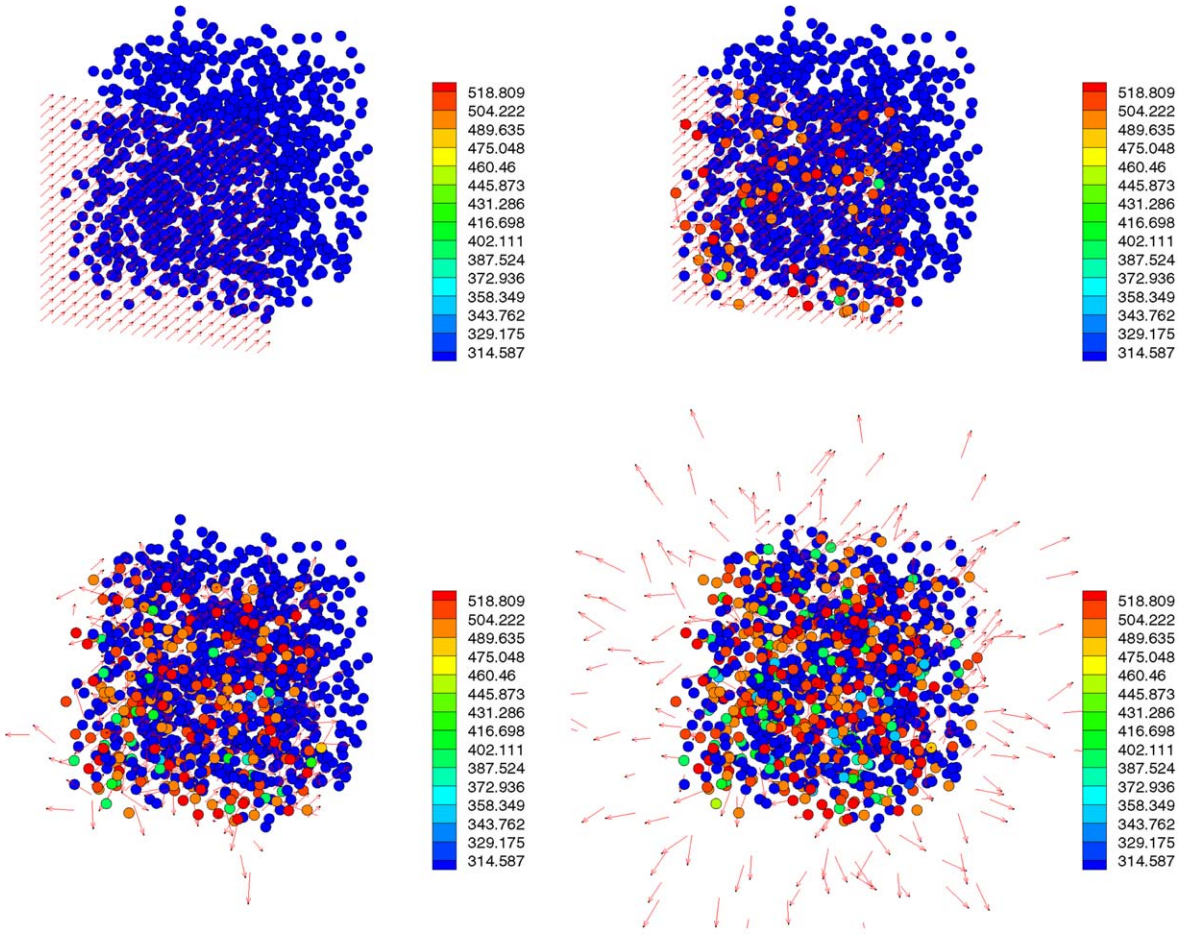

Fig. 7. Starting from left to right and top to bottom, the progressive movement of rays comprising a beam (for the best inverse parameter set vector (Table 1)). The colors of the particles indicate their temperature and the length of the vectors indicate the irradiance magnitude.

strings per parameter selection for the ensemble averaging stabilization. After approximately 6 generations, the procedure stabilized. We again remark that gradient-based methods are sometimes useful for post-processing solutions found with a genetic algorithm, if the objective function is sufficiently smooth in that region of the parameter space. This was not done in this work, however, the reader can consult the texts of Luenberger [45] and Gill et al. [21], or the survey in [54].

6. Concluding remarks and future work

The presented work developed a ray-tracing algorithm, which was combined with a stochastic genetic algorithm, in order to treat coupled inverse optical scattering formulations, where physical parameters, such as particulate volume fractions, refractive indices and thermal constants, were sought so that the overall response of a sample of randomly distributed particles, suspended in an ambient medium, would match desired coupled scattering, thermal and infrared responses. Large-scale numerical simulations were presented to illustrate the overall procedure and to investigate aggregate ray dynamics corresponding to the flow of electromagnetic energy and the conversion of the absorbed energy into heat and infrared radiation through disordered particulate systems.

Such design methodologies may be helpful in design of optical coating materials comprised of randomly dispersed particles suspended in a binding matrix. The matrix usually has good adhesive and mechanical properties, while the particles are used as scattering units. Such coatings are relatively inexpensive to fabricate. The overall optical properties of such materials can be tailored by adjusting the volume fraction and refractive index of the particulate additives.

Accordingly, one can consider a more detailed description of the scatterers, where we characterize the shape of the particles by a generalized ellipsoidal equation:[7]

$$F \overset{\text{def}}{=} \left(\frac{|x-x_0|}{r_1}\right)^{s_1} + \left(\frac{|y-y_0|}{r_2}\right)^{s_2} + \left(\frac{|z-z_0|}{r_3}\right)^{s_3} = 1, \tag{6.1}$$

[7] The outward surface normals, $\boldsymbol{n}$, needed during the scattering calculations, are relatively easy to characterize by writing $\boldsymbol{n} = \frac{\nabla F}{\|\nabla F\|}$.

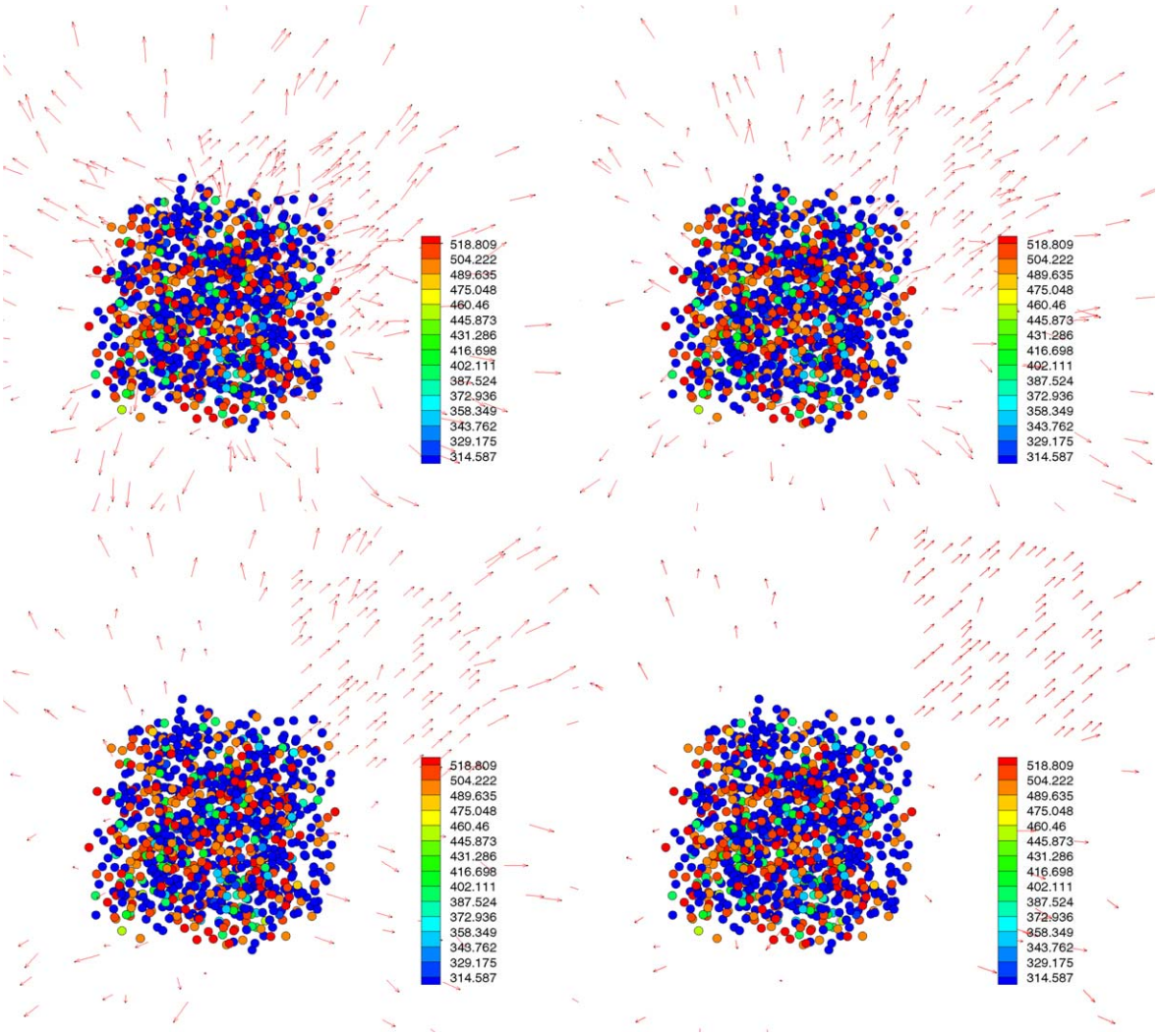

Fig. 8. Continuing Fig. 7. Starting from left to right and top to bottom, the progressive movement of rays comprising a beam (for the best inverse parameter set vector (Table 1)). The colors of the particles indicate their temperature and the length of the vectors indicate the irradiance magnitude.

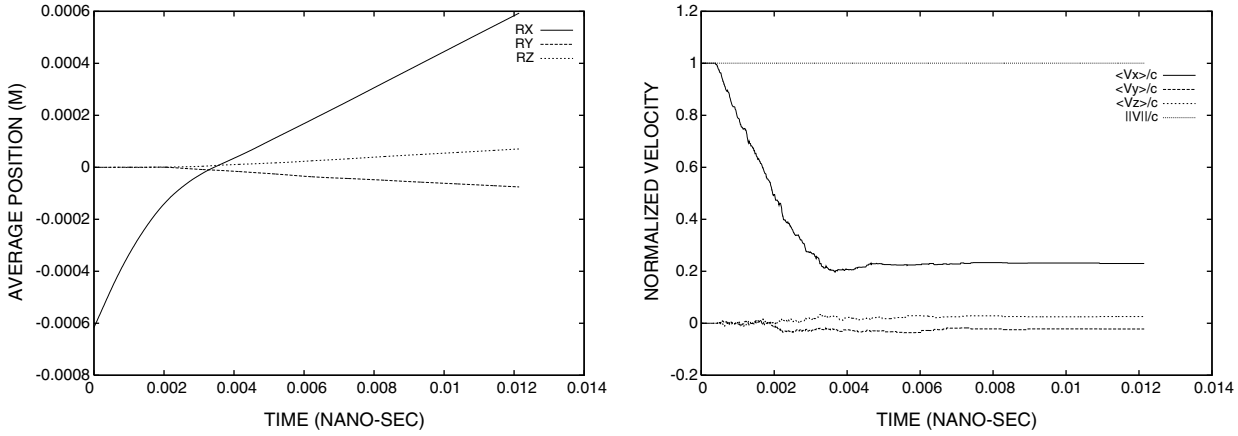

Fig. 9. Left: The components of the average position over time for the best parameter set. Right: The components of the average ray velocity and the Euclidean norm over time for the best parameter set. The normalized quantity, $\|\mathbf{v}\|/c = 1$, which serves as a error check.

where the s's are exponents. The orientation of the particles, usually random, can be controlled, via rotational coordinate transformations. Values of $s < 1$ produce nonconvex shapes, while $s > 2$ values produce "block-like" shapes (three inverse-

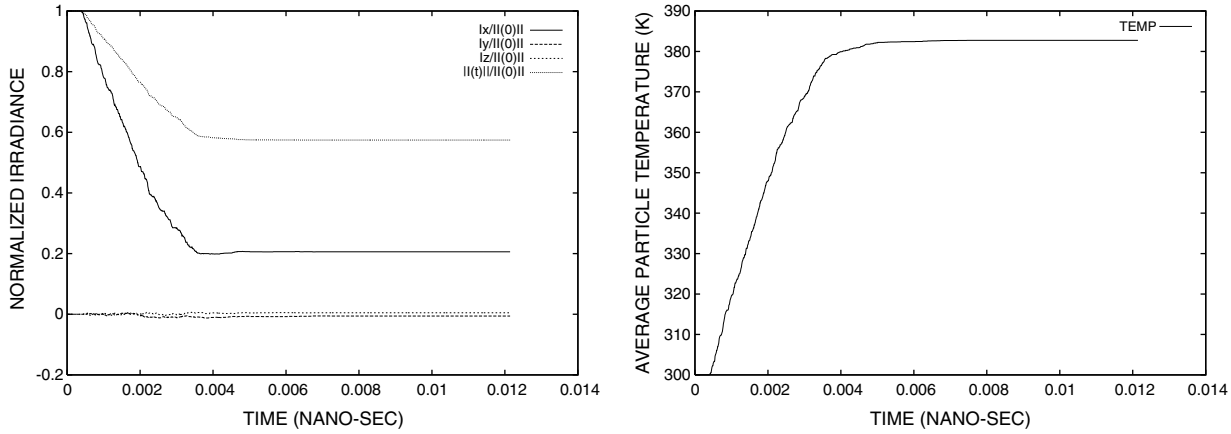

Fig. 10. Left: The components of the average ray irradiance and the Euclidean norm over time for the best parameter set. Right: The average temperature of the scatterers over time for the best parameter set.

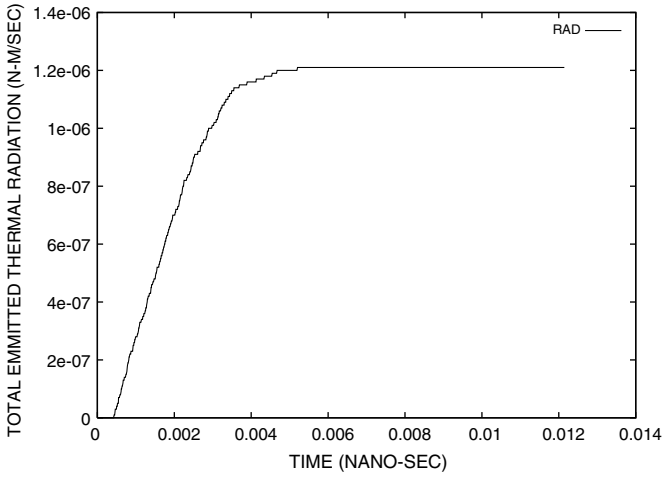

Fig. 11. The average thermal radiation of the scatterers over time for the best parameter set.

parameters). Furthermore, we can introduce particulate aspect ratio, defined by $AR \stackrel{\text{def}}{=} \frac{r_1}{r_2} = \frac{r_1}{r_3}$, where $r_2 = r_3$, $AR > 1$ for prolate geometries and $AR < 1$ for oblate shapes (one variable). Therefore, including the variables introduced before, in the most general case we have a total of nine variables, $\mathbf{\Lambda} = (\mathscr{L}, \rho C, \epsilon, \hat{n}, \hat{\mu}, s_1, s_2, s_3, AR)$. We remark that if the particles' orientations are assumed aligned, then three more (angular orientation) parameters can be introduced, $(\theta_1, \theta_2, \theta_3)$. In fact, suspensions can become aligned, for example, along electrical field lines induced by external sources, or due to flow conditions. Thus, the search space grows to 12 parameters,[8] $\mathbf{\Lambda} = (\mathscr{L}, \rho C, \epsilon, \hat{n}, \hat{\mu}, s_1, s_2, s_3, AR, \theta_1, \theta_2, \theta_3)$.

Finally, in addition to a more detailed characterization of the particle geometry, in some cases transparent particle materials, accounting for refractive and dispersive rays traveling through scatterers can be important. Recall that the dispersion of a light ray is the manner in which, for example, white light, which is a mixture of all wavelengths of visible light, can be decomposed into its constituent wavelengths or colors when it passes from one medium into another. This phenomena occurs because the index of refraction of a transparent medium is greater for light of shorter wavelengths. Thus, whenever light is refracted in passing from one medium to the next, the violet and blue light of shorter wavelengths is bent more than the orange and red light of longer wavelengths.[9] Thus, dispersive effects introduce a new level of complexity, primarily because of the refraction of different wavelengths of light, leading to a dramatic growth in the number of rays of varying intensities and color (wavelength). The inclusion of these effects is under current investigation by the author.

[8] It is important to note that the control of the particle properties, volume fractions, orientations, etc., can be used to design hybrid thin films composed of particulate additives in a matrix binder.

[9] This is how a rainbow is formed.

Appendix A. Maxwell's equations

To understand the propagation of electromagnetic waves it is necessary to employ Maxwell's equations in a form relating the electric and magnetic field vectors (following Telford et al. [58]):

$$\nabla \times \boldsymbol{E} = -\frac{\partial \boldsymbol{B}}{\partial t} \quad \text{and} \quad \nabla \times \boldsymbol{H} = \boldsymbol{J} + \frac{\partial \boldsymbol{D}}{\partial t}, \tag{A.1}$$

where $\boldsymbol{J}$ is the current density (A/m^2), $\boldsymbol{E}$ is the electric field intensity (V/m), $\boldsymbol{B}$ is the magnetic flux density (tesla, T), $\boldsymbol{H}$ is the magnetic flux intensity (A/m) and $\boldsymbol{D}$ is the electric displacement (C/m^2). Using the vector identity $\nabla \cdot (\nabla \times \boldsymbol{A}) = 0$, we obtain

$$\nabla \cdot (\nabla \times \boldsymbol{E}) = -\nabla \cdot \frac{\partial \boldsymbol{B}}{\partial t} = -\frac{\partial \nabla \cdot \boldsymbol{B}}{\partial t} = 0 \;\Rightarrow\; \nabla \cdot \boldsymbol{B} = 0 \tag{A.2}$$

and

$$\nabla \cdot (\nabla \times \boldsymbol{H}) = \nabla \cdot \left(\boldsymbol{J} + \frac{\partial \boldsymbol{D}}{\partial t} \right) = \nabla \cdot \boldsymbol{J} + \frac{\partial \nabla \cdot \boldsymbol{D}}{\partial t} = 0. \tag{A.3}$$

The divergence of the current density is equivalent to the rate of accumulation of the charge density, denoted Q, thus

$$\nabla \cdot \boldsymbol{J} = -\frac{\partial Q}{\partial t} = -\frac{\partial \nabla \cdot \boldsymbol{D}}{\partial t} = 0 \;\Rightarrow\; \nabla \cdot \boldsymbol{D} = Q. \tag{A.4}$$

In regions of finite conductivity, charge does not accumulate during current flow, hence $Q = 0$ so that

$$\nabla \cdot \boldsymbol{J} = 0 \quad \text{and} \quad \nabla \cdot \boldsymbol{D} = \epsilon \nabla \cdot \boldsymbol{E} = 0, \tag{A.5}$$

where ϵ is the dielectric permittivity. In addition the relation between displacement and electric field, for a homogeneous isotropic medium, we also have the following constitutive relation between $\boldsymbol{B}$ and $\boldsymbol{H}$

$$\boldsymbol{B} = \mu \boldsymbol{H}, \tag{A.6}$$

where μ is the magnetic permeability of the medium, and Ohm's law

$$\boldsymbol{D} = \epsilon \boldsymbol{E} \quad \text{and} \quad \boldsymbol{J} = \sigma \boldsymbol{E}, \tag{A.7}$$

where σ is the conductivity, and where, for convenience, the free space parameters have been absorbed into the medium's parameter definitions. Thus, we may write

$$\nabla \times \boldsymbol{E} = -\mu \frac{\partial \boldsymbol{H}}{\partial t} \quad \text{and} \quad \nabla \times \boldsymbol{H} = \sigma \boldsymbol{E} + \epsilon \frac{\partial \boldsymbol{E}}{\partial t}. \tag{A.8}$$

In some situations, there are independent current sources, $\boldsymbol{J}^s$, not related to the magnetic field (for example, from power devices), and we may write

$$\nabla \times \boldsymbol{H} = \boldsymbol{J}^s + \sigma \boldsymbol{E} + \epsilon \frac{\partial \boldsymbol{E}}{\partial t} = 0. \tag{A.9}$$

Applying the vector identity[10]

$$\nabla \times (\nabla \times \boldsymbol{A}) = \nabla (\nabla \cdot \boldsymbol{A}) - \nabla^2 \boldsymbol{A}, \tag{A.10}$$

we obtain

$$\nabla^2 \boldsymbol{E} = \mu \frac{\partial}{\partial t} (\nabla \times \boldsymbol{H}) = \mu \sigma \frac{\partial \boldsymbol{E}}{\partial t} + \mu \epsilon \frac{\partial^2 \boldsymbol{E}}{\partial t^2} \tag{A.11}$$

and

$$\nabla^2 \boldsymbol{H} = -\sigma (\nabla \times \boldsymbol{E}) - \epsilon \frac{\partial}{\partial t} (\nabla \times \boldsymbol{E}) = \mu \sigma \frac{\partial \boldsymbol{H}}{\partial t} + \mu \epsilon \frac{\partial^2 \boldsymbol{H}}{\partial t^2}. \tag{A.12}$$

If we choose time-harmonic sinusoidal time variations

$$\boldsymbol{E}(t) = \boldsymbol{E}_0 \mathrm{e}^{\mathrm{j}\omega t} \quad \text{and} \quad \boldsymbol{H}(t) = \boldsymbol{H}_0 \mathrm{e}^{\mathrm{j}\omega t} \tag{A.13}$$

thus

$$\frac{\partial \boldsymbol{E}}{\partial t} = \mathrm{j}\omega \boldsymbol{E} \quad \text{and} \quad \frac{\partial \boldsymbol{H}}{\partial t} = \mathrm{j}\omega \boldsymbol{H}, \tag{A.14}$$

[10] Note, using the vector identity $\nabla \cdot (\nabla \times \boldsymbol{A}) = 0$ we have $\nabla \cdot \boldsymbol{H} = 0$ and $\nabla \cdot \boldsymbol{E} = 0$.

where $\omega = 2\pi f$ is the angular frequency of the field, we may write

$$\nabla^2 \boldsymbol{E} = \mathrm{j}\omega\mu\sigma\boldsymbol{E} - \omega^2\mu\epsilon\boldsymbol{E} \quad \text{and} \quad \nabla^2 \boldsymbol{H} = \mathrm{j}\omega\mu\sigma\boldsymbol{H} - \omega^2\mu\epsilon\boldsymbol{H}. \tag{A.15}$$

These are the equations for the time-harmonic propagation of electric and magnetic field vectors in an isotropic homogeneous medium having conductivity σ, permeability of μ and permittivity of ϵ.

Importantly, at an interface, the following must hold:

- the electric field tangential to the interface must be continuous: $\boldsymbol{n} \times (\boldsymbol{E}_1 - \boldsymbol{E}_2) = \boldsymbol{0}$,
- the magnetic field tangential to the interface must be continuous: $\boldsymbol{n} \times (\boldsymbol{H}_1 - \boldsymbol{H}_2) = \boldsymbol{0}$,
- the current density normal to the interface must be continuous: $\boldsymbol{n} \cdot (\sigma_1\boldsymbol{E}_1 - \sigma_2\boldsymbol{E}_2) = 0$,
- the magnetic flux normal to the interface must be continuous: $\boldsymbol{n} \cdot (\mu_1\boldsymbol{H}_1 - \mu_2\boldsymbol{H}_2) = 0$.

These relations are valid when there is no free charge or current on the interface. All electromagnetic fields must satisfy these relations at all interfaces. See Telford et al. [58] for more details.

References

[1] R.P. Behringer, The dynamics of flowing sand, Nonlinear Sci. Today 3 (1993) 1.
[2] R.P. Behringer, G.W. Baxter, Pattern formation, complexity & time-dependence in granular flows, in: A. Mehta (Ed.), Granular Matter—An Interdisciplinary Approach, Springer-Verlag, New York, 1993, pp. 85–119.
[3] R.P. Behringer, B.J. Miller, Stress fluctuations for sheared 3D granular materials, in: R. Behringer, J. Jenkins (Eds.), Proceedings, Powders & Grains 97, Balkema, Amsterdam, 1997, pp. 333–336.
[4] R.P. Behringer, D. Howell, C. Veje, Fluctuations in granular flows, Chaos 9 (1999) 559–572.
[5] Y.A. Berezin, K. Hutter, L.A. Spodareva, Stability properties of shallow granular flows, Int. J. Nonlinear Mech. 33 (4) (1998) 647–658.
[6] C. Bohren, D. Huffman, Absorption and Scattering of Light by Small Particles. Wiley Science Paperback Series, 1998.
[7] T.T. Charalampopoulos, G. Shu, Optical properties of combustion-synthesized iron oxide aggregates, Appl. Opt. 42 (19) (2003) 3957–3969.
[8] T.T. Charalampopoulos, G. Shu, Effects of polydispersity of chainlike aggregates on light-scattering properties and data inversion, Appl. Opt. 41 (4) (2002) 723–733.
[9] A. Chokshi, A.G.G.M. Tielens, D. Hollenbach, Dust coagulation, Astrophys. J. 407 (1993) 806–819.
[10] L. Davis, Handbook of Genetic Algorithms, Thompson Computer Press, 1991.
[11] C. Dominik, A.G.G.M. Tielens, The physics of dust coagulation & the structure of dust aggregates in space, Astrophys. J. 480 (1997) 647–673.
[12] A. Donev, I. Cisse, D. Sachs, E.A. Variano, F. Stillinger, R. Connelly, S. Torquato, P. Chaikin, Improving the density of jammed disordered packings using ellipsoids, Science 303 (February) (2004) 990–993.
[13] A. Donev, S. Torquato, F. Stillinger, Neighbor list collision-driven molecular dynamics simulation for nonspherical hard particles—I. Algorithmic details, J. Comput. Phys. 202 (2005) 737.
[14] A. Donev, S. Torquato, F. Stillinger, Neighbor list collision-driven molecular dynamics simulation for nonspherical hard particles—II: Application to ellipses and ellipsoids, J. Comput. Phys. 202 (2005) 765.
[15] W.C. Elmore, M.A. Heald, Physics of Waves, Dover Publications re-issue, 1985.
[16] A. Kansaal, S. Torquato, F. Stillinger, Diversity of order and densities in jammed hard-particle packings, Phys. Rev. E 66 (2002) 041109.
[17] J.M.N.T. Gray, M. Wieland, K. Hutter, Gravity-driven free surface flow of granular avalanches over complex basal topography, Proc. R Soc. Lond. A 455 (1999) 1841–1874.
[18] J.M.N.T. Gray, K. Hutter, Pattern formation in granular avalanches, Continuum Mech. Thermodyn. 9 (1997) 341–345.
[19] J.M.N.T. Gray, Granular flow in partially filled slowly rotating drums, J. Fluid Mech. 441 (2001) 1–29.
[20] J.H. Holland, Adaptation in Natural & Artificial Systems, Ann Arbor, Mich. University of Michigan Press, 1975.
[21] P. Gill, W. Murray, M. Wright, Practical optimization, Academic Press, London, 1995.
[22] D.E. Goldberg, Genetic algorithms in search, optimization & machine learning, Addison-Wesley, Reading, MA, 1989.
[23] D.E. Goldberg, K. Deb, in: Special issue on Genetic Algorithms, Comput. Methods Appl. Mech. Engrg. 186 (2–4) (2000) 121–124.
[24] R. Greve, K. Hutter, Motion of a granular avalanche in a convex & concave curved chute: experiments & theoretical predictions, Philos. Trans. R Soc. Lond. A 342 (1993) 573–600.
[25] K. Hutter, Avalanche dynamics, in: V.P. Singh (Ed.), Hydrology of Disasters, Kluwer Academic Publishers, Dordrecht, 1996, pp. 317–394.
[26] K. Hutter, T. Koch, C. Plüss, S.B. Savage, The dynamics of avalanches of granular materials from initiation to runout. Part II. Experiments, Acta Mech. 109 (1995) 127–165.
[27] K. Hutter, K.R. Rajagopal, On flows of granular materials, Continuum Mech. Thermodynam. 6 (1994) 81–139.
[28] K. Hutter, M. Siegel, S.B. Savage, Y. Nohguchi, Two-dimensional spreading of a granular avalanche down an inclined plane. Part I: Theory, Acta Mech. 100 (1993) 37–68.
[29] H.M. Jaeger, S.R. Nagel, La Physique de l'Etat Granulaire, La Recherche 249 (1992) 1380.
[30] H.M. Jaeger, S.R. Nagel, Physics of the granular state, Science 255 (1992) 1523.
[31] H.M. Jaeger, S.R. Nagel, La Fisica del Estado Granular, Mundo Cientifico 132 (1993) 108.
[32] H.M. Jaeger, J.B. Knight, C.H. Liu, S.R. Nagel, What is shaking in the sand box? Mater. Res. Soc. Bull. 19 (1994) 25.
[33] H.M. Jaeger, S.R. Nagel, R.P. Behringer, The physics of granular materials, Phys. Today 4 (1996) 32.
[34] H.M. Jaeger, S.R. Nagel, R.P. Behringer, Granular solids, liquids & gases, Rev. Mod. Phys. 68 (1996) 1259.
[35] H.M. Jaeger, S.R. Nagel, Dynamics of granular material, Am. Sci. 85 (1997) 540.
[36] J.T. Jenkins, O.D.L. Strack, Mean-field inelastic behavior of random arrays of identical spheres, Mech. Mater. 16 (1993) 25–33.
[37] J.T. Jenkins, L. Ragione, La particle spin in anisotropic granular materials, Int. J. Solids Struct. 38 (1999) 1063–1069.

[38] J.T. Jenkins, M.A. Koenders, The incremental response of random aggregates of identical round particles, Eur. Phys. J. E—Soft Matter. 13 (2004) 113–123.
[39] J.T. Jenkins, D. Johnson, L. La Ragione, H. Makse, Fluctuations and the effective moduli of an isotropic, random aggregate of identical, frictionless spheres, J. Mech. Phys. Solids 53 (2005) 197–225.
[40] J. Kennedy, R. Eberhart, Swarm Intelligence, Morgan Kaufmann Publishers, Los Altos, CA, 2001.
[41] T. Koch, R. Greve, K. Hutter, Unconfined flow of granular avalanches along a partly curved surface. II. Experiments & numerical computations, Proc. R Soc. Lond. A 445 (1994) 415–435.
[42] N. Lagaros, M. Papadrakakis, G. Kokossalakis, Structural optimization using evolutionary algorithms, Comput. Struct. 80 (2002) 571–589.
[43] C.H. Liu, H.M. Jaeger, S.R. Nagel, Finite size effects in a sandpile, Phys. Rev. A 43 (1991) 7091.
[44] C.H. Liu, S.R. Nagel, Sound in a granular material: disorder & nonlinearity, Phys. Rev. B 48 (1993) 15646.
[45] D. Luenberger, Introduction to Linear and Nonlinear Programming, Addison-Wesley, Menlo Park, 1974.
[46] P. Mitchell, M. Frenklach, Particle aggregation with simultaneous surface growth, Phys. Rev. E 67 (2003) 061407.
[47] S.R. Nagel, Instabilities in a sandpile, Rev. Modern Phys. 64 (1992) 321.
[48] J.F. Nye, Physical Properties of Crystals, Oxford University Press, Oxford, 1957.
[49] C. Onwubiko, Introduction to Engineering Design Optimization, Prentice Hall, Englewood Cliffs, NJ, 2000.
[50] M. Papadrakakis, N. Lagaros, G. Thierauf, J. Cai, Advanced solution methods in structural optimisation using evolution strategies, Engrg. Comput. J. 15 (1) (1998) 12–34.
[51] M. Papadrakakis, N. Lagaros, Y. Tsompanakis, Structural optimization using evolution strategies and neutral networks, Comput. Methods Appl. Mech. Engrg. 156 (1) (1998) 309–335.
[52] M. Papadrakakis, N. Lagaros, Y. Tsompanakis, Optimization of large-scale 3D trusses using evolution strategies and neural networks, Int. J. Space Struct. 14 (3) (1999) 211–223.
[53] M. Papadrakakis, J. Tsompanakis, N. Lagaros, Structural shape optimisation using evolution strategies, Enrg. Optim. 31 (1999) 515–540.
[54] M. Papadrakakis, N. Lagaros, Y. Tsompanakis, V. Plevris, Large scale structural optimization: computational methods and optimization algorithms, Arch. Comput. Methods Engrg. State Art Rev. 8 (3) (2001) 239–301.
[55] Y.-C. Tai, S. Noelle, J.M.N.T. Gray, K. Hutter, Shock capturing & front tracking methods for granular avalanches, J. Comput. Phys. 175 (2002) 269–301.
[56] Y.-C. Tai, J.M.N.T. Gray, K. Hutter, S. Noelle, Flow of dense avalanches past obstructions, Ann. Glaciol. 32 (2001) 281–284.
[57] Y.-C. Tai, S. Noelle, J.M.N.T. Gray, K. Hutter, An accurate shock-capturing finite-difference method to solve the Savage–Hutter equations in avalanche dynamics, Ann. Glaciol. 32 (2001) 263–267.
[58] W.M. Telford, L.P. Geldart, R.E. Sheriff, Applied Geophysics, second ed., Cambridge University Press, Cambridge, 1990.
[59] S. Torquato, Random Heterogeneous Materials: Microstructure and Macroscopic Properties, Springer-Verlag, New York, 2002.
[60] H.C. van de Hulst, Light Scattering by Small Particles, Dover Publications re-issue, 1981.
[61] B. Widom, Random sequential addition of hard spheres to a volume, J. Chem. Phys. 44 (1966) 3888–3894.
[62] M. Wieland, J.M.N.T. Gray, K. Hutter, Channelized free-surface flow of cohesionless granular avalanches in a chute with shallow lateral curvature, J. Fluid Mech. 392 (1999) 73–100.
[63] T.I. Zohdi, An adaptive-recursive staggering strategy for simulating multifield coupled processes in microheterogeneous solids, Int. J. Numer. Methods Engrg. 53 (2002) 1511–1532.
[64] T.I. Zohdi, Computational design of swarms, Int. J. Numer. Methods Engrg. 57 (2003) 2205–2219.
[65] T.I. Zohdi, Modeling and simulation of a class of coupled thermo-chemo-mechanical processes in multiphase solids, Comput. Methods Appl. Mech. Engrg. 193 (6–8) (2004) 679–699.
[66] T.I. Zohdi, Genetic optimization of statistically uncertain microheterogeneous solids, Philos. Trans. R Soc. Math. Phys. Engrg. Sci. 361 (1806) (2003) 1021–1043.
[67] T.I. Zohdi, Modeling and direct simulation of near-field granular flows, Int. J. Solids Struct. 42 (2) (2004) 539–564.
[68] T.I. Zohdi, A computational framework for agglomeration in thermo-chemically reacting granular flows, Proc. R Soc. 460 (2004) 3421–3445.
[69] T.I. Zohdi, Charge-induced clustering in multifield granular flow, Int. J. Numer. Methods Engrg. 62 (7) (2005) 870–898.